

# Paramagnetic relaxation in sandstones: Distinguishing $T_1$ and $T_2$ dependence on surface relaxation, internal gradients and dependence on echo spacing <sup>☆</sup>

Vivek Anand <sup>a,\*</sup>, George J. Hirasaki <sup>b</sup>

<sup>a</sup> Schlumberger Product Center, 125 Industrial Boulevard, MD 125-01, Sugar Land, TX 77478, USA

<sup>b</sup> Chemical and Biomolecular Engineering Department, Rice University, Houston, TX 77005, USA

Received 11 June 2007; revised 20 September 2007

Available online 4 October 2007

## Abstract

This work provides a generalized theory of proton relaxation in inhomogeneous magnetic fields. Three asymptotic regimes of relaxation are identified depending on the shortest characteristic time scale. Numerical simulations illustrate that the relaxation characteristics in the regimes such as the  $T_1/T_2$  ratio and echo spacing dependence are determined by the time scales. The theoretical interpretation is validated for fluid relaxation in porous media in which field inhomogeneity is induced due to susceptibility contrast of fluids and paramagnetic sites on pore surfaces. From a set of measurements on model porous media, we conclude that when the sites are small enough, no dependence on echo spacing is observed with conventional low-field NMR spectrometers. Echo spacing dependence is observed when the paramagnetic materials become large enough or form a ‘shell’ around each grain such that the length scale of the region of induced magnetic gradients is large compared to the diffusion length during the time of the echo spacing. The theory can aid in interpretation of diffusion measurements in porous media as well as imaging experiments in presence of contrast agents used in MRI.

© 2007 Elsevier Inc. All rights reserved.

**Keywords:** Paramagnetic relaxation; Internal field; Susceptibility; Porous media; Contrast agents

## 1. Introduction

Inhomogeneous magnetic fields are employed for several applications in NMR relaxometry and imaging. For example, field gradients of the order of 10–100 T/m are applied in Stray Field Imaging for high resolution of systems with broad line widths [1–4]. Functional MRI utilizes the inhomogeneous field induced by paramagnetic contrast agents for increasing sensitivity and specificity [5,6]. The field gradient generated by oil well-logging tools is utilized for identification of hydrocarbons in earth’s formation [7,8].

In this paper, we provide a theoretical and experimental framework for understanding proton relaxation in inho-

mogeneous magnetic fields. Field inhomogeneity can be applied externally or induced internally within the system due to difference in magnetic susceptibility of constituents. Diffusion of fluid molecules in inhomogeneous fields leads to additional relaxation of transverse magnetization due to loss of phase coherence. The additional relaxation is called “secular relaxation” [9] and is defined as the difference in transverse and longitudinal relaxation rates.

$$\frac{1}{T_{2,\text{sec}}} = \frac{1}{T_2} - \frac{1}{T_1} \quad (1)$$

We focus on secular relaxation in water-saturated porous media although the theory is applicable for any system in which inhomogeneous fields are present.

At present, there is no exact theory which explains secular relaxation in porous media in a general inhomogeneous field. However, two ideal cases of relaxation in a constant gradient and relaxation in an inhomogeneous field induced by

<sup>☆</sup> Paper was presented at 48th Annual Symposium of Society of Petrophysicists and Well Log Analysts.

\* Corresponding author. Fax: +1 281 285 8071.

E-mail address: [vanand@slb.com](mailto:vanand@slb.com) (V. Anand).

paramagnetic spheres have been described analytically in the past. DeSwiet et al. [10] described three length scales that characterize secular relaxation in a constant gradient  $g$ :

- (1) Pore structural length,  $L_s$
- (2) Diffusion length,  $L_d$ , defined as

$$L_d = \sqrt{D\tau_E} \quad (2)$$

where  $D$  is the diffusivity of the fluid and  $\tau_E$  is the echo spacing for CPMG pulse sequence

- (3) Dephasing length,  $L_g$ , defined as the distance over which the spins have to diffuse in order to dephase by 1 radian given as

$$L_g = \sqrt[3]{\frac{D}{\gamma g}} \quad (3)$$

where  $\gamma$  is the proton gyromagnetic ratio. Depending on the smallest length scale, secular relaxation can be characterized into three relaxation regimes of motionally averaging, free diffusion and localization. Similarly, secular relaxation in the field induced by paramagnetic spheres has been classified into regimes of motionally averaging, weak magnetization and strong magnetization depending on three characteristic time scales [9,11,12]. Analytical expressions for secular relaxation rates have been proposed for the different asymptotic regimes.

This study proposes a generalized relaxation theory which extends the definition of the asymptotic regimes defined for the ideal case of diffusion in a constant gradient to general inhomogeneous fields. The regimes are determined by the shortest characteristic time scale [11], which can be defined for a general inhomogeneous field, rather than the smallest length scale. The time scales also quantify the characteristics of the relaxation regimes such as echo spacing dependence and  $T_1/T_2$  ratio.

The paper is organized as follows. In Section 2, the generalized theory of secular relaxation in inhomogeneous fields is provided. The theory is independent of the particular choice of the inhomogeneous field distribution. Section 3 illustrates the dependence of characteristic time scales in sedimentary rocks on governing parameters such as the concentration and the size of paramagnetic particles. Section 4 describes random walk simulations of the secular relaxation in the field induced by paramagnetic spheres to quantitatively illustrate the characteristics of the relaxation regimes. Sections 5 and 6 describe a series of NMR measurements that physically explore relaxation regimes in porous media.

## 2. Generalized secular relaxation theory

### 2.1. Characteristic time scales for secular relaxation

Transverse relaxation due to dephasing in magnetic field inhomogeneities is characterized by three time scales [11]:

- (1) time taken for significant dephasing,  $\tau_\omega$ , defined as the inverse of the spread in Larmor frequencies ( $\delta\omega$ ) existing in the system

$$\tau_\omega = \frac{1}{\delta\omega} \quad (4)$$

- (2) diffusional correlation time,  $\tau_R$ , defined as the time taken to diffusively average the inhomogeneities

$$\tau_R = \frac{L^2}{D} \quad (5)$$

where  $L$  is the characteristic length of field inhomogeneity in the system, and

- (3) half echo spacing used in CPMG pulse sequence,  $\tau_E$ , given as

$$\tau_E = \frac{TE}{2} \quad (6)$$

where  $TE$  is the echo spacing for the CPMG sequence.

The length scale of the field inhomogeneity ( $L$ ) and spread in Larmor frequencies ( $\delta\omega$ ) depend on particular system parameters. For example, let us consider the characteristic time scales for two cases of relaxation in a constant gradient and in the field induced by paramagnetic spheres.

1. Restricted diffusion in a constant gradient: For the case of restricted diffusion in a constant gradient  $g$  in a pore, field inhomogeneity exists over the entire length of the pore. Therefore, the diffusional correlation time and time for significant dephasing are given as

$$\tau_R = \frac{L_s^2}{D} \quad (7)$$

$$\tau_\omega = \frac{1}{\delta\omega} = \frac{1}{\gamma g L_s} \quad (8)$$

where  $L_s$  is the structural length of the pore.

2. Relaxation in the field induced by a paramagnetic sphere: A paramagnetic particle of magnetic susceptibility different from that of the surrounding medium induces magnetic field inhomogeneities when placed in an external magnetic field. Potential theory can be used to estimate the induced fields in idealized geometries. The component of the field induced by a paramagnetic sphere along the direction of the external field  $\vec{B}_0$  is given as [13]

$$B_{\delta z} = B_0 \left( \frac{k-1}{k+2} \right) (3 \cos^2 \theta - 1) \frac{R_0^3}{r^3} \quad (9)$$

where  $R_0$  is the radius of the sphere,  $k = (1 + \chi_{\text{sphere}})/(1 + \chi_{\text{medium}})$ ,  $\chi_{\text{sphere}}$  and  $\chi_{\text{medium}}$  are magnetic susceptibilities of the sphere and the medium respectively.  $\theta$  is the azimuthal angle from the direction of  $\vec{B}_0$ , and  $r$  is the radial distance from the center of the paramagnetic sphere. The component of the induced field along the external magnetic

field is considered since this component determines the precession frequency. Eq. (9) shows that the induced field is maximum at the surface of the sphere (positive at poles and negative at equator) and falls as the cube of the radial distance from the center. Thus, the range of Larmor frequencies in the system is the difference in polar and equatorial fields at the surface of the sphere given as

$$\delta\omega = \frac{3(k-1)}{(k+2)}\gamma B_0 \quad (10)$$

$\tau_\omega$  is given by the reciprocal of  $\delta\omega$ . In addition, field inhomogeneity extends to distances proportional to the radius of the sphere. Thus,  $\tau_R$  is given as

$$\tau_R = \frac{R_0^2}{D} \quad (11)$$

## 2.2. Asymptotic regimes of secular relaxation

Depending on the shortest characteristic time scale, secular relaxation in inhomogeneous fields can be characterized by three regimes of motionally averaging, free diffusion and localization. A description of the regimes is provided in this section. For each regime, the cases of relaxation in a constant gradient and relaxation in the field induced by paramagnetic spheres are also included. It is instructive to note that even though the two systems have very different field distribution, the relaxation rates in a particular regime are similar when expressed in terms of characteristic time scales. This correspondence proves that the time scales are the governing parameters that describe relaxation in inhomogeneous fields.

*Motionally averaging regime:* The motionally averaging regime is characterized by fast diffusion of protons such that the inhomogeneities in magnetic field are motionally averaged [9]. This averaging occurs when the diffusional correlation time is much shorter compared to the half echo spacing and the time taken for significant dephasing due to field inhomogeneities. Thus, the conditions of motionally averaging regime are

$$\begin{aligned} \tau_R &\ll \tau_\omega \\ \tau_R &\ll \tau_E \end{aligned} \quad (12)$$

1. Motionally averaging regime in a constant gradient: The conditions for motionally averaging in a constant gradient in a pore of length  $L_s$  can be obtained in terms of the characteristic length scales (Eqs. (2) and (3)) by substituting Eqs. (7) and (8) in Eq. (12) given as

$$\begin{aligned} L_s &\ll L_g \\ L_s &\ll L_d \end{aligned} \quad (13)$$

Eq. (13) imply that the motionally averaging regime is observed when the pore structural length is small compared to the diffusion length during time  $\tau_E$  ( $L_d$ ) and the dephasing length ( $L_g$ ). Thus, the spins typically

diffuse several times the pore size during the measurement and any magnetic field inhomogeneities are averaged by their motion.

Neumann [14] derived the expression for the secular relaxation rate in the motionally averaging regime by assuming the distribution of phase shifts to be Gaussian given as

$$\frac{1}{T_{2,\text{sec}}} = \frac{L_s^4 \gamma^2 g^2}{120D} \quad (14)$$

Using Eqs. (7) and (8), Eq. (14) can be expressed in terms of characteristic parameters as shown

$$\frac{1}{T_{2,\text{sec}}} = \frac{1}{120} \delta\omega^2 \tau_R \quad (15)$$

Thus, the relaxation rate is independent of the echo spacing and shows a quadratic dependence on field inhomogeneity ( $\delta\omega$ ) in the motionally averaging regime. This quadratic dependence on field inhomogeneity was also derived for a non-constant field gradient in one-dimensional restricted geometry by Tarczón et al. [15].

2. Motionally averaging regime in internal fields induced by paramagnetic spheres: Motionally averaging regime for relaxation by paramagnetic spheres arises when the diffusional correlation time (Eq. (11)) is the shortest time scale. Thus, the conditions for motionally averaging regime in terms of system parameters are

$$\begin{aligned} \frac{R_0^2}{D} &\ll \tau_E \\ \frac{R_0^2}{D} &\ll \tau_\omega = \frac{1}{\delta\omega} = \frac{(k+2)}{3(k-1)\gamma B_0} \end{aligned} \quad (16)$$

The expression for  $\delta\omega$  in Eq. (16) is substituted from Eq. (10). The quantum-mechanical outer sphere theory suggests that when conditions for motionally averaging are satisfied, the secular relaxation rate is given as [9]

$$\frac{1}{T_{2,\text{sec}}} = \frac{16}{405} \Phi \delta\omega^2 \tau_R = \frac{16}{45D} \Phi \left( \frac{(k-1)}{(k+2)} \gamma B_0 R_0 \right)^2 \quad (17)$$

where  $\Phi$  is the volume fraction of the paramagnetic particles. Eq. (17) is derived by solving quantum-mechanical equations for the “flip rates” of the protons using time dependent perturbation theory [9]. Note the similar functional form of the secular relaxation rate predicted by the outer sphere theory (Eq. 17) and Eq. 15.

*Free diffusion regime:* This regime is valid when the half echo spacing is the shortest characteristic time scale. The effect of restriction as well as large field inhomogeneities is not felt by the spins in the time of echo formation. Thus, the spins dephase as if diffusing in an unrestricted medium. The conditions for the free diffusion regime are

$$\begin{aligned} \tau_E &\ll \tau_\omega \\ \tau_E &\ll \tau_R \end{aligned} \quad (18)$$

1. Free diffusion in a constant gradient: For the case of diffusion in a constant gradient in a pore, the free diffusion regime may arise for small echo spacing such that the spins do not experience the restriction effects in the time of echo formation. The conditions for free diffusion inside a pore of length  $L_s$  can be obtained in terms of the characteristic length scales by substituting Eqs. (7) and (8) in Eq. (18) given as

$$\begin{aligned} L_d &\ll L_g \\ L_d &\ll L_s \end{aligned} \quad (19)$$

Thus, the free diffusion regime arises when the diffusion distance in  $\tau_E$  is much smaller compared to the dephasing length and the pore length. In this regime, the secular relaxation rate is given by the classical expression derived by Carr and Purcell [16] for unrestricted diffusion in a constant gradient

$$\frac{1}{T_{2,\text{sec}}} = \frac{\gamma^2 g^2 \tau_E^2 D}{3} \quad (20)$$

Substituting Eqs. (4)–(6) in Eq. (20), the relaxation rate in constant gradient can be written as

$$\frac{1}{T_{2,\text{sec}}} = \frac{\delta\omega^2 \tau_E^2}{3\tau_R} \quad (21)$$

2. Free diffusion in internal fields induced by paramagnetic spheres: The free diffusion regime has been described as the “weak magnetization regime ( $\delta\omega \cdot \tau_E < 1$ )” in the magnetic resonance imaging (MRI) literature mentioned below. The regime arises physically when weakly magnetized paramagnetic particles are used as contrast agents for medical imaging or in biological tissues with iron rich cells or deoxygenated red blood cells [17]. Brooks et al. [11] calculated the mean squared gradient of the magnetic field induced by a paramagnetic sphere given as

$$\langle g^2 \rangle = \frac{4\Phi\delta\omega^2}{5\gamma^2 R_0^2} \quad (22)$$

Substituting Eq. (22) in the expression for the relaxation rate in unrestricted diffusion (Eq. (20)) and accounting for restriction from neighboring particles, the relaxation rate in the presence of weakly magnetized spheres is given as [11]

$$\frac{1}{T_{2,\text{sec}}} = \frac{\Phi\delta\omega^2 \tau_E^2}{5\tau_R} = \frac{9\Phi}{5} \left[ \frac{(k-1)}{(k+2)} \gamma B_0 \right]^2 \frac{\tau_E^2 D}{R_0^2} \quad (23)$$

The above expression (called the Mean Gradient Diffusion Theory, MGDТ) shows the similar quadratic dependence of secular relaxation rate on the echo spacing as the expression for unrestricted diffusion in a constant gradient (Eq. (21)). However, the relaxation rate shows an inverse squared dependence on the paramagnetic particle size which is opposite to that in the motionally averaging regime (Eq. (17)). This inverse dependence arises because

the mean squared field gradient in Eq. (22) decreases as the square of the particle size.

*Localization regime:* Localization regime of secular relaxation arises when the dephasing time is the shortest time scale. The conditions for the localization regime are

$$\begin{aligned} \tau_\omega &\ll \tau_R \\ \tau_\omega &\ll \tau_E \end{aligned} \quad (24)$$

1. Localization regime in a constant gradient: Using Eqs. (7) and (8) for  $\delta\omega$  and  $\tau_R$  for restricted diffusion in a constant gradient in a pore of length  $L_s$ , Eq. (24) reduces to the following equations in special cases

$$\begin{aligned} L_g &\ll L_d \\ L_g &\ll L_s \end{aligned} \quad (25)$$

Thus, the dephasing length ( $L_g$ ) is the smallest characteristic length in the localization regime. The spins typically dephase to such an extent during the measurement time that they do not contribute to the total magnetization. The signal comes primarily from the spins near the boundaries which see smaller change in the magnetic field due to reflection [18]. DeSwiet et al. [10] have shown that at long times, the echo amplitude in the localization regime decays as

$$\frac{M(g, \tau_E)}{M_0} = c \left( \frac{D}{\gamma g L_s^3} \right)^{1/3} e^{-a_1 (D\gamma^2 g^2 \tau_E^3)^{1/3}} \quad (26)$$

where  $a_1 = 1.0188\dots$  and  $c = 5.8841\dots$  for parallel plates.

2. Localization regime in internal fields induced by paramagnetic spheres: Secular relaxation in the localization regime has also been discussed in the MRI literature. The regime arises physically for relaxation in presence of strongly magnetized contrast agents such as superparamagnetic particles for which  $\delta\omega\tau_E > 1$ . Gillis et al. [12] proposed a semi-empirical model for decay in internal fields induced by strongly magnetized spheres. In their model, the region surrounding the paramagnetic sphere is divided into two regions: an inner region with very strong internal gradients and an outer region with only weak gradients. Since the gradients in the outer region are weak, Gillis et al. [12] suggested that relaxation in the outer region can be described by theory for weakly magnetized particles. Thus, the relaxation rate in the outer region is given by Eq. (23) with a modification to account for the excluded volume of the inner region as shown below

$$\frac{1}{T_{2,\text{sec}}} = \frac{\Phi\delta\omega^2 \tau_E^2}{5\tau_R} \left( \frac{\delta\omega\tau_E}{a + b\Phi\delta\omega\tau_E} \right)^{-5/3} \quad (27)$$

The values of the parameters  $a$  ( $=4.5$ ) and  $b$  ( $=0.99$ ) were calculated by Gillis et al. [12] by fitting Eq. (27) to numerical simulations of transverse relaxation in the presence of strongly magnetized spheres.

In the inner region, the spins experience strong gradients and dephase very rapidly. Due to rapid dephasing, they do not contribute significantly to the macroscopic relaxation rate; therefore Eq. (27) provides an accurate estimate of relaxation rate in presence of strongly magnetized particles.

### 3. Relaxation regimes in sandstones

The previous section described the classification of secular relaxation in asymptotic regimes depending on the characteristic time scales. We can obtain physical insight of the different regimes by considering the example of secular relaxation of fluids in sandstones. Sedimentary rocks usually contain paramagnetic minerals such as iron on the surfaces of silica grains [19]. Thus, the relaxation of pore fluids can be influenced by field inhomogeneities induced due to susceptibility differences between pore fluids and the paramagnetic minerals. For the case of paramagnetic relaxation in sedimentary rocks, the characteristic time scales depend not only on the size and susceptibility of paramagnetic particles but also on the concentration of particles and the size of silica grains. The two cases of dilute and high surface concentrations of the paramagnetic particles are described below.

#### 3.1. Paramagnetic particles at dilute surface concentration

At low concentrations of paramagnetic particles on silica surfaces, there is negligible superposition of the fields induced by individual particles. Fig. 1 shows the contour plots of the longitudinal component of the internal field

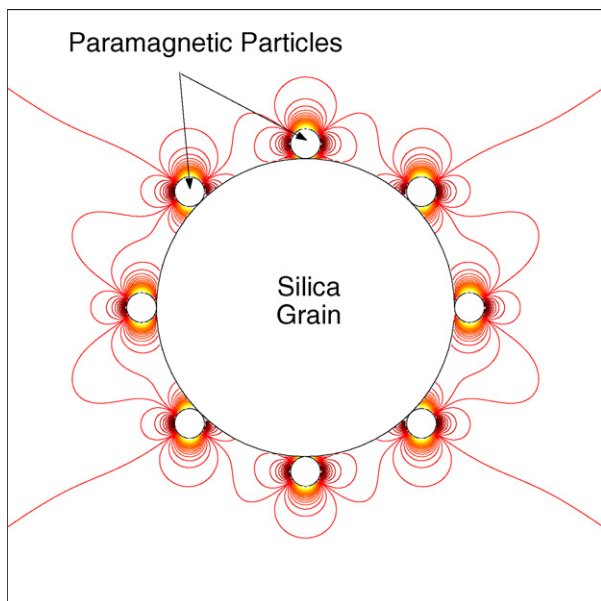


Fig. 1. Contour plots of induced magnetic field in the outer region of a silica grain coated with paramagnetic spheres at dilute concentrations (No. of particles per unit area  $\sim 3$ ). The ratio of the radius of the silica grain to that of paramagnetic particles is 10. At low concentrations, there is insignificant superposition of fields induced by neighboring particles.

in the outer region of a silica grain coated with paramagnetic spheres at dilute concentration. The particles are separated far enough from each other such that the field induced by one particle is not significantly influenced by the fields induced by neighboring particles. Due to insignificant superposition, the protons in the outer region of the grain dephase as if diffusing in an internal field induced by a single paramagnetic sphere. Thus, the asymptotic regimes mentioned for a single sphere are applicable for describing secular relaxation in sandstones with dilute paramagnetic concentration. The spread in Larmor frequency ( $\delta\omega$ ) and diffusional correlation time ( $\tau_R$ ) are given by Eqs. (10) and (11) defined for a single paramagnetic sphere.

#### 3.2. Paramagnetic particles at high surface concentration

At high surface concentration of paramagnetic particles, the internal fields induced by individual particles overlap. Thus, the inhomogeneous field extends to larger distances than at lower surface concentrations due to superposition. Fig. 2 shows the contour plots of the internal field in the outer region of a grain coated with paramagnetic spheres at high concentration. Strong field gradients are induced close to the surface of the particles. In addition, the fields induced by neighboring particles superpose and extend to a length scale comparable to the size of the substrate silica grain.

At high concentrations, the particles can be visualized as forming a paramagnetic “shell” around the silica grain.

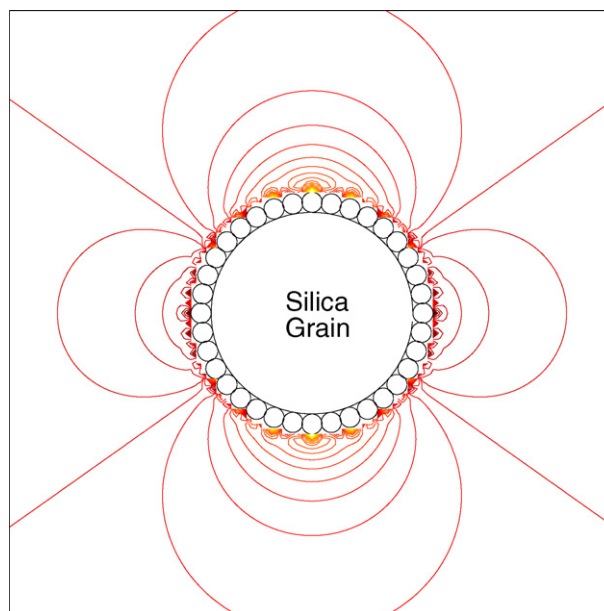


Fig. 2. Contour plots of magnetic field in the outer region of a silica grain coated with paramagnetic spheres at high concentrations (No. of particles per unit area  $\sim 30$ ). The ratio of radius of the silica grain to that of paramagnetic particles is 10. At high concentrations, induced field extends to distance proportional to the radius of the silica grain due to superposition of fields induced by neighboring particles.

Consider a grain of radius  $R_g$  coated with a paramagnetic shell of thickness  $\varepsilon$ . The internal field induced by the paramagnetic shell can be calculated by subtracting the field induced by a sphere of radius  $R_g$  from the field induced by a concentric sphere of radius  $R_g + \varepsilon$ . Thus, the internal field contribution of only the spherical shell survives. Using Eq. (9) for the field induced by a paramagnetic sphere, the field distribution for a paramagnetic shell is given as

$$B_{\delta z} = \frac{(k-1)B_0(3\cos^2\theta-1)}{(k+2)} \left[ \frac{(R_g + \varepsilon)^3}{r^3} - \frac{R_g^3}{r^3} \right], \quad r > R_g + \varepsilon \quad (28)$$

$$\approx \frac{(k-1)B_0(3\cos^2\theta-1)}{(k+2)} \frac{3\varepsilon R_g^2}{r^3}, \quad \varepsilon \ll R_g$$

Similar to the field distribution of a solid sphere (Eq. (9)), the field is maximum at the surface of the shell (positive at poles and negative at equator) and falls as the cube of the radial distance. Thus, the range of Larmor frequencies is the difference in polar and equatorial frequencies at the surface given as

$$\delta\omega_{\text{shell}} \approx \frac{(k-1)\gamma B_0}{(k+2)} \frac{9\varepsilon}{R_g} \quad (29)$$

The frequency range ( $\delta\omega_{\text{shell}}$ ) is proportional to the ratio of the thickness of the paramagnetic shell to the radius of the silica grain. As a validation of this relationship, consider the limiting case of the field induced by an infinite paramagnetic sheet ( $R_g \rightarrow \infty$ ). A paramagnetic sheet perpendicular to an externally applied field does not induce any field gradients since the field lines still remain parallel. This is also quantitatively verified by Eq. (29) which shows  $\delta\omega_{\text{shell}} \rightarrow 0$  as  $R_g \rightarrow \infty$ .

Eq. (29) shows that the frequency range for a paramagnetic shell decreases by a factor  $3\varepsilon/R_g$  in comparison to that for a single solid sphere (Eq. (10)). Thus, the time for significant dephasing ( $\tau_\omega$ ) increases by the same factor. In addition, the field inhomogeneity extends to a length scale comparable to the size of the substrate silica grain. Thus, for a close-packing structure of silica grains in sandstones, the length scale of field inhomogeneity ( $L$ ) is proportional to the dimension of the interstitial pore between the grains given as [20]

$$L = 0.225R_g \quad (30)$$

Therefore,  $\tau_R$  increases as the square of the silica grain radius rather than the paramagnetic particle radius. For sufficiently coarse grained sandstones,  $\tau_R$  can become larger than  $\tau_\omega$ . Hence, the system can experience the localization regime (if  $\tau_\omega < \tau_E$ ) or the free diffusion regime (if  $\tau_E < \tau_\omega$ ) even if silica grains are coated with fine-sized paramagnetic particles.

In addition to  $\delta\omega$ , the paramagnetic volume fraction ( $\Phi$ ) also changes at the transition from an individual particle at low concentration to a shell at high concentrations. At low concentrations,  $\Phi$  is the ratio of the volume of the para-

magnetic particles to the total volume. However, at high concentrations,  $\Phi$  corresponds to the solid matrix volume fraction since the particles cover the surface of silica grains. The condition for transition from individual particle at low concentration to a paramagnetic shell at high concentration is

$$(\delta\omega\Phi)_{\text{particle}} = (\delta\omega\Phi)_{\text{shell}} \quad (31)$$

This condition ensures that the secular relaxation rates vary smoothly at the transition.

#### 4. Random walk simulations

The relaxation rates of Section 2 are valid only in asymptotic regions of the parameter space spanned by the three characteristic time scales. To provide a quantitative understanding of secular relaxation in the entire parameter space, random walk simulations are performed. Secular relaxation in an inhomogeneous field induced in the annular region outside a paramagnetic sphere is modeled. This model is chosen because relaxation rates in asymptotic regions of the parameter space are known analytically. Few simplifying assumptions are made. Surface relaxation at the inner radius ( $R_0$ ) and the outer radius ( $R_e$ ) of the annulus is neglected. It is also assumed that spin-echoes are measured by CPMG pulse sequence with ideal pulses. The theory is presented in terms of dimensionless quantities so that the results are invariant under changes in particular system parameters.

##### 4.1. Governing Bloch–Torrey equations

The relaxation of transverse magnetization ( $M$ ) in an inhomogeneous field  $B_z$  after the application of the first  $\pi/2$  pulse is given by the Bloch–Torrey equation

$$\frac{\partial M}{\partial t} = -i\gamma B_z M - \frac{M}{T_{2,B}} + D\nabla^2 M \quad (32)$$

where  $D$  is the diffusivity of the fluid and  $T_{2,B}$  is the bulk relaxation time. By substituting  $M = M_x + iM_y$  and  $M = m \cdot e^{\left(-i\omega_0 t + \frac{t}{T_{2,B}}\right)}$ , Eq. (32) can be expressed as

$$\frac{\partial m}{\partial t} = -i\gamma B_{\delta z} m + D\nabla^2 m \quad (33)$$

Here  $m$  represents the transverse magnetization with the precession at the Larmor frequency ( $\omega_0 = \gamma B_0$ ) and the bulk relaxation factored out [21].  $B_{\delta z}$  ( $=B_z - B_0$ ) is the component of the internal field along the direction of the externally applied field.

The following dimensionless variables are introduced to normalize Eq. (33)

$$r^* = \frac{r}{R_e}, \quad t^* = \frac{t}{t_0}, \quad m^* = \frac{m}{M_0}$$

where  $t_0$  is a characteristic time and  $M_0$  is the initial magnetization. Substituting the dimensionless variables and

Eq. (9) for the internal field induced by a paramagnetic sphere in Eq. (33), the following dimensionless equation is obtained

$$\frac{\partial m^*}{\partial t^*} = -i \frac{(3 \cos^2 \theta - 1)}{r^{*3}} \left( \frac{\gamma B_0 (k-1)}{(k+2)} \left( \frac{R_0}{R_c} \right)^3 t_0 \right) m^* + N_D \nabla^{*2} m^* \quad (34)$$

where dimensionless group  $N_D$  is defined as

$$N_D = \frac{Dt_0}{R_c^2} \quad (35)$$

The characteristic time  $t_0$  is chosen such that the coefficient of the second term in Eq. (34) is unity. Thus,

$$t_0 = \left[ \frac{(k+2)}{\gamma B_0 (k-1)} \right] \frac{1}{\Phi} \quad (36)$$

where  $\Phi$  is the volume fraction of the paramagnetic particle given as

$$\Phi = \left( \frac{R_0}{R_c} \right)^3 \quad (37)$$

Using Eq. (10) for the frequency range ( $\delta\omega$ ) of the inhomogeneous field induced by the paramagnetic sphere,  $t_0$  can also be expressed as

$$\Rightarrow t_0 = \frac{3}{\Phi \delta\omega} \quad (38)$$

Eq. (38) is used to normalize secular relaxation rates for the experimental systems as described in Section 6. The dimensionless parameter,  $N_D$ , can be expressed in terms of system parameters by substituting Eq. (36) in Eq. (35)

$$N_D = \frac{Dt_0}{R_c^2} = \frac{(k+2)DR_c}{(k-1)\gamma B_0 R_c^3} = \frac{3}{(\delta\omega\tau_R)\Phi^{1/3}} \quad (39)$$

Eq. (39) shows that  $N_D$  is *not* an independent dimensionless group but is specified if two dimensionless parameters  $\delta\omega\tau_R$  and  $\Phi$  are specified. Thus, the governing Bloch equation in dimensionless form becomes

$$\frac{\partial m^*}{\partial t^*} = -i \frac{(3 \cos^2 \theta - 1)}{r^{*3}} m^* + N_D \nabla^{*2} m^* \quad (40)$$

No surface relaxation at the inner and outer boundary implies

$$\frac{\partial m^*}{\partial r^*} = 0 \quad \text{at } r^* = 1 \text{ and } r^* = \frac{R_0}{R_c} \quad (41)$$

In addition, the application of  $\pi$  pulse at dimensionless half echo spacing  $\tau_E^*$  reverses the y component of the magnetization. Thus,

$$m^*|_{t^*} = \overline{m^*}|_{t^*+} \quad (42)$$

at  $t^* = \tau_E^*, 3\tau_E^*, 5\tau_E^* \dots$  where the dimensionless half echo spacing,  $\tau_E^*$ , is given as

$$\tau_E^* = \tau_E/t_0 \quad (43)$$

A continuous random walk algorithm [22] is applied to numerically integrate the dimensionless equations. Secular relaxation of protons in the field induced by a paramagnetic sphere of susceptibility 0.2 (SI units) surrounded by a medium of susceptibility  $-0.8 \times 10^{-6}$  (SI units) is simulated. These values of susceptibilities are representative of magnetite and water respectively. The external magnetic field  $B_0$  corresponds to a proton Larmor frequency of 2 MHz. The radius of the paramagnetic sphere is varied from 10 nm to 25  $\mu\text{m}$ . For each particle size, simulations with several values of  $\tau_E$  are performed to illustrate the echo spacing dependence of secular relaxation in different regimes. The dimensionless relaxation rate is calculated from the slope of exponential fit to the simulated echo intensities. However, the magnetization decay is multi-exponential for simulations such that  $\delta\omega\tau_R > 1000$ . For such cases, the relaxation rate is calculated from the slowest component of the multi-exponential decay. The details of the algorithm are mentioned in the Appendix.

## 4.2. Results and discussion

Secular relaxation can be classified in three asymptotic regimes (Section 2) depending on two dimensionless parameters: normalized diffusional correlation time  $\delta\omega\tau_R$ , and normalized echo spacing  $\delta\omega\tau_E$ . Fig. 3 shows the plot of simulated dimensionless relaxation rates ( $1/T_{2,\text{sec}}^D$ ) as a function of  $\delta\omega\tau_R$  for different values of  $\delta\omega\tau_E$ . The superscript ‘‘D’’ refers to the dimensionless relaxation rate.  $\delta\omega$  and  $\tau_R$  are calculated from Eqs. (10) and (11) respectively for the specified values of radius and susceptibility of the paramagnetic sphere. The plots of theoretical relaxation

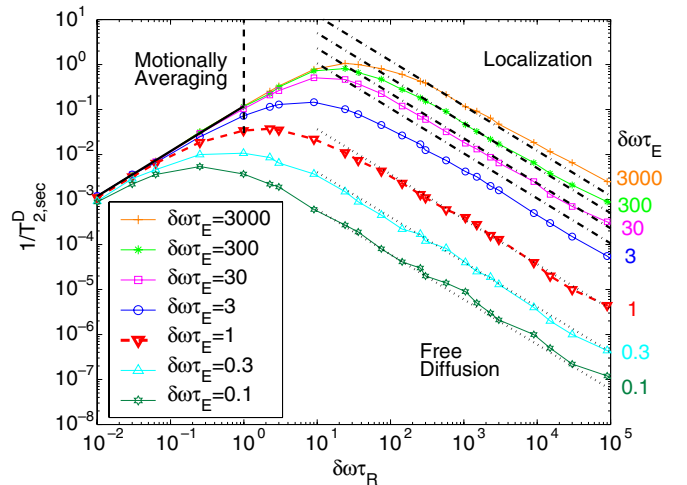


Fig. 3. Plot of simulated relaxation rate (dimensionless) with  $\delta\omega\tau_R$  as a function of  $\delta\omega\tau_E$ . The parameters used in the simulations are  $\Phi = 1.25 \times 10^{-4}$ ,  $k = 1.2$ ,  $B_0 = 496$  G. The solid, dotted and dash-dotted lines are the theoretically estimated secular relaxation rates according to the outer sphere theory (Eq. (17)), mean gradient diffusion theory (Eq. (23)) and modified mean gradient diffusion theory (Eq. (27)) plotted in the respective regimes of validity. The dashed lines are the boundaries  $\delta\omega\tau_R = 1$  and  $\delta\omega\tau_E = 1$  that delineate the asymptotic regimes.

rates are also shown for comparison in the respective regimes of validity. Thus the solid, dotted and dash-dotted lines are the plots of theoretical relaxation rates (Eqs. (17), (23), (27)) normalized by the characteristic rate  $1/t_0$ . The dashed lines are the boundaries  $\delta\omega\tau_R = 1$  and  $\delta\omega\tau_E = 1$  that delineate the asymptotic regimes. Note that the relaxation rates can be made dimensional by using the following equation.

$$\frac{1}{T_{2,\text{sec}}} = \frac{1}{t_0 T_{2,\text{sec}}^D} = \left[ \frac{(k-1)\gamma B_0 \Phi}{(k+2)} \right] \frac{1}{T_{2,\text{sec}}^D} \quad (44)$$

The characteristics of secular relaxation rate in Fig. 3 can be described in terms of the three regimes:

1. *Motionally averaging regime*: Motionally averaging regime exists for  $\delta\omega\tau_R \ll 1$  and sufficiently large values of  $\delta\omega\tau_E \gg 1$ . In this regime, secular relaxation rates are independent of the echo spacing because the field inhomogeneities are averaged in time much shorter compared to  $\tau_E$ . In addition, the rates increase with  $\tau_R$  and thus, with the particle size. A physical understanding for the dependence of relaxation rate on  $\tau_R$  can be obtained by considering the chemical exchange (CE) model of transverse relaxation [23–25]. The CE model consists of two sites A and B with a frequency shift ( $\delta\omega$ ) between them and the protons are chemically exchanging between the sites with an exchange time  $\tau_{\text{ex}}$ . The phenomenon of transverse relaxation due to chemical exchange between sites is analogous to secular relaxation due to diffusion between continuous spectrum of frequencies in the random walk model. The presence of only two discrete chemical shifts and no diffusion contribution makes the integration of Bloch equation in the CE model easier. Thus, physical insight about secular relaxation can be gained by analyzing the relaxation rates predicted by the CE model. The fraction of protons in the two sites is given by  $F_A$  and  $F_B$  respectively. When  $F_B \ll 1$ , the relaxation rate is given as [24]

$$\frac{1}{T_2} = F_B \tau_{\text{ex}} \frac{(\delta\omega)^2}{(1 + (\delta\omega)^2 \tau_{\text{ex}}^2)} \quad (45)$$

In motionally averaging regime ( $\delta\omega\tau_{\text{ex}} \ll 1$ ) of the CE model, Eq. (45) reduces to

$$\frac{1}{T_2} \cong F_B \tau_{\text{ex}} (\delta\omega)^2 \quad (46)$$

When  $\delta\omega \ll 1/\tau_{\text{ex}}$ , exchange of protons between the two sites is fast compared to the dephasing rate. Thus, the rate determining step is the amount of dephasing in the exchange time  $\tau_{\text{ex}}$ . As  $\tau_{\text{ex}}$  increases, the protons in the two sites are dephased by a larger amount and hence, the relaxation rates increase with  $\tau_{\text{ex}}$  as shown by Eq. (46).

As mentioned earlier, this CE model is analogous to the relaxation model in outer region of a paramagnetic sphere. The protons may be considered either near the

sphere (site B) where there is a frequency shift of order  $\delta\omega$  or far away where there is no shift (site A). The exchange time from site B to site A is proportional to the diffusional correlation time which is the time to diffuse the length scale of field inhomogeneity. Thus, when diffusional exchange between the two sites is fast compared to dephasing rate (i.e. motionally averaging,  $\delta\omega \ll 1/\tau_R$ ), relaxation rates increase with  $\tau_R$  similar to the predictions of the CE model.

2. *Localization regime*: Localization regime exists for  $\delta\omega\tau_R \gg 1$  and large values of  $\delta\omega\tau_E \gg 1$ . In this regime, the relaxation rates show strong dependence on the echo spacing. Additionally, the dependence of the relaxation rate on  $\tau_R$  (and thus, the particle size) is inverted in contrast to that in the motionally averaging regime. The CE model also provides an explanation for the decrease in relaxation rates with particle size in the localization regime. When the condition  $\delta\omega\tau_{\text{ex}} \gg 1$  holds, Eq. (45) reduces to

$$\frac{1}{T_2} \cong \frac{F_B}{\tau_{\text{ex}}} \quad (47)$$

Thus, the relaxation rates are inversely proportional to  $\tau_{\text{ex}}$  in contrast to Eq. (46) for the motionally averaging regime. For  $\delta\omega \gg 1/\tau_{\text{ex}}$ , dephasing rate is much larger compared to the rate at which protons exchange between sites A and B. Due to large dephasing, the protons are lost from the signal in a single exchange from site A to site B [26]. Thus, the relaxation rate is determined by the rate at which protons exchange between the two sites i.e.  $1/\tau_{\text{ex}}$ . For relaxation by paramagnetic spheres, a similar inverse dependence of relaxation rates on  $\tau_R$  (which is analogous to  $\tau_{\text{ex}}$ ) is observed when  $\delta\omega\tau_R \gg 1$ .

The simulated relaxation rates in the localization regime of Fig. 3 match well with the predictions of modified MGD (Eq. (27)) except at large values of  $\delta\omega\tau_E$  and  $\delta\omega\tau_R$ . This deviation is probably because at large values of parameters  $\delta\omega\tau_E$  and  $\delta\omega\tau_R$ , the contribution of the inner region to the overall decay becomes substantial. Thus, the assumption that the decay is only governed by outer region in the derivation of Eq. (27) may not be entirely valid.

3. *Free diffusion regime*: Free diffusion regime exists for small echo spacings such that  $\delta\omega\tau_E \ll 1$  and  $\delta\omega\tau_E \ll \delta\omega\tau_R$ . Due to effective refocusing by  $\pi$  pulses in the free diffusion regime, the simulated relaxation rates are significantly smaller than the ones in localization or motionally averaging regimes. For  $\delta\omega\tau_R > 1$ , the relaxation rates show inverse dependence on the particle size similar to that in the localization regime.

The above mentioned characteristics of the asymptotic regimes can be easily visualized in the  $(\delta\omega\tau_R, \delta\omega\tau_E)$  parameter space. Fig. 4 shows contour plots (solid curves) of simulated dimensionless relaxation rates in the  $(\delta\omega\tau_R, \delta\omega\tau_E)$  domain. The contour plots differ by a factor of  $\sqrt{10}$ .

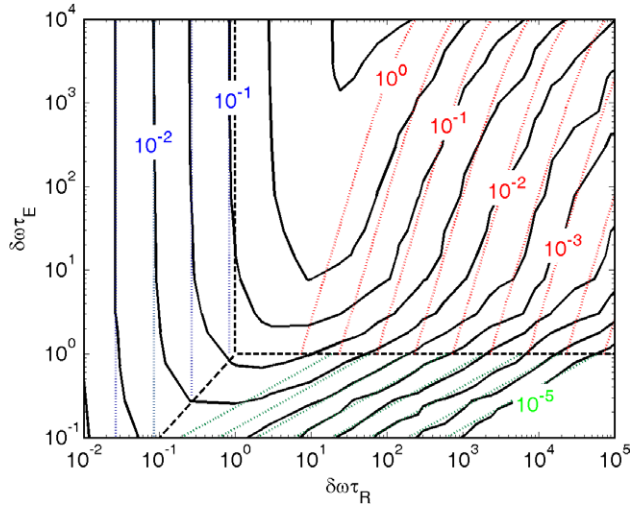


Fig. 4. Contour plots of dimensionless secular relaxation rate in the  $(\delta\omega\tau_R, \delta\omega\tau_E)$  parameter space. The contours differ by a factor of  $\sqrt{10}$ . The parameters used in the simulations are same as for Fig. 3. The dotted lines are the corresponding plots for theoretically predicted relaxation rates given by Eqs. (17), (23) and (27). The bold dashed lines are boundaries between asymptotic regimes. The contours are invariant for dilute volume fractions ( $\Phi \leq 1.25 \times 10^{-4}$ ).

Corresponding plots (dotted curves) for the theoretically predicted relaxation rates given by Eqs. (17), (23) and (27) are also shown in respective regions of validity. The boundaries between the asymptotic regimes are shown by dashed lines. In the motionally averaging regime ( $\delta\omega\tau_R \ll 1, \delta\omega\tau_E \gg 1$ ), the contour plots are almost parallel to the  $\delta\omega\tau_E$  axis implying that the relaxation rates are independent of the echo spacing. Also, the rates increase with  $\delta\omega\tau_R$  showing that the secular relaxation increases with particle size. In localization and free diffusion regimes, the dependence of relaxation on  $\delta\omega\tau_R$  is reversed and the rates decrease with particle size. In addition, the rates are echo spacing dependent in these regimes. The contours are more closely spaced and have lesser slope in the free diffusion regime than in the localization regime. Thus, the dependence of the relaxation rate on the echo spacing is higher in the free diffusion regime than in the localization regime.

The echo spacing dependence of relaxation rates in the free diffusion and the localization regime can also be quantified. Fig. 5 shows the plot of simulated relaxation rates with  $\delta\omega\tau_E$  for cases in which  $\delta\omega\tau_R \gg 1$ . The dashed line shows the boundary  $\delta\omega\tau_E = 1$  between free diffusion and localization regimes. The dotted and dash-dotted lines are theoretically predicted relaxation rates in the two regimes (Eqs. (23) and (27)). Relaxation rates show quadratic dependence on the echo spacing in the free diffusion regime as predicted by Eq. (23). However, the slopes of relaxation rates decrease as the systems transition from the free diffusion to the localization regime. Power-law fits of relaxation rates with  $\delta\omega\tau_E$  in the localization regime show that the exponent of  $\tau_E$  is approximately unity for low values of  $\delta\omega\tau_E$  ( $1 \leq \delta\omega\tau_E \leq 15$ ) and decreases to less than 0.6 for lar-

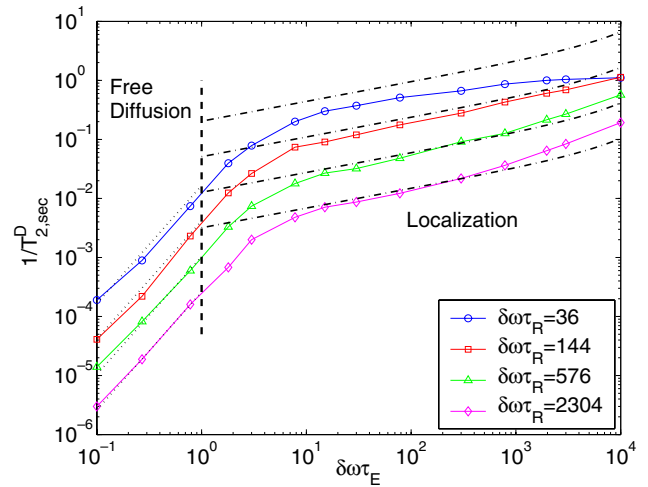


Fig. 5. Plot of secular relaxation rates (dimensionless) with dimensionless echo spacing  $\delta\omega\tau_E$  for  $\delta\omega\tau_R \gg 1$ . The dotted and dash-dotted lines are theoretically predicted relaxation rates in the free diffusion and the localization regime given by Eqs. (23) and (27), respectively. The bold dashed line is the boundary  $\delta\omega\tau_E = 1$  delineating free diffusion and localization regimes. The dependence of relaxation rates on the echo spacing is quadratic in the free diffusion regime and less than quadratic in the localization regime.

ger values of  $\delta\omega\tau_E$  ( $10^2 \leq \delta\omega\tau_E \leq 10^3$ ). Thus, these simulations show that non-quadratic dependence of relaxation rates on the echo spacing can result in the localization regime as has also been observed experimentally by several researchers [27,28].

Since the theory is presented in dimensionless terms, the plots in Figs. 3–5 are invariant under changes in parameters such as magnetic susceptibility of the paramagnetic sphere, diffusivity of the fluid, external magnetic field, etc. However, the relaxation rates are invariant under changes in volume fraction for only dilute volume fractions ( $\Phi \leq 1.25 \times 10^{-4}$ ). Simulations for different volume fractions show that the average absolute deviation is less than 10% for  $\Phi < 10^{-3}$ . For  $\Phi = 0.6$ , the average absolute deviation is greater than 50% [29].

## 5. Experimental

This section experimentally illustrates the characteristics of secular relaxation in porous media. We first describe NMR measurements with aqueous dispersions of paramagnetic particles of known sizes. These experiments help to quantitatively estimate the characteristic time scales for the paramagnetic particles. Next we describe NMR measurements with model sandstones synthesized by coating the paramagnetic particles on silica grains. These model systems simulate secular relaxation in sedimentary rocks in which field inhomogeneities are often induced due to the presence of paramagnetic minerals and clays. Thus, a conceptual understanding of paramagnetic relaxation in porous media is developed based on theoretical and experimental results.

### 5.1. Paramagnetic particles in aqueous dispersions

1. *Ferric ion*: The smallest paramagnetic particle studied was ferric ion (hydrated ionic diameter = 0.12 nm [20]). Solutions of ferric chloride were prepared at various solute concentrations in 0.1 N Hydrochloric acid. Acidic pH of the solutions prevents the formation of ferric hydroxide. Proton longitudinal and transverse relaxation of the solutions was measured at 2 MHz and 30 °C. Fig. 6 shows  $T_1$  and  $T_2$  relaxation rates of the aqueous solution of ferric ions as a function of the solution concentration. The relaxation rates of the solutions increase linearly with the concentration. Furthermore, the  $T_1/T_2$  ratio is unity and no echo spacing dependence of the transverse relaxation is observed.  $T_1/T_2$  ratio of unity suggests that the secular relaxation does not contribute significantly to the transverse relaxation for ferric ion solutions. This assertion is validated by the calculation of characteristic time scales shown later.
2. *Magnetite nanoparticles coated with citrate ion*: To explore a larger length scale of field inhomogeneity, positively charged magnetite nanoparticles of different sizes were synthesized in aqueous medium using Massart's Method [30]. The aim of synthesizing positively charged nanoparticles is to adsorb them on the negatively charged silica surface by columbic attraction. Thus, relaxation characteristics of model sandstones with paramagnetic particles adsorbed at different concentrations can be studied.

The following experimental procedure was used to synthesize aqueous dispersions of magnetite nanoparticles. Ammonia solution was added dropwise to an aqueous mixture of ferrous and ferric chloride till a gelatinous precipitate (magnetite) was obtained. The precipitated magnetite was washed with Perchloric acid which makes the particles positively charged due to surface adsorption of protons. The charged particles can then be dispersed in excess water [30]. The size of the particles can be controlled by changing the temperature of the reaction. Larger particles are obtained at higher temperatures due to increased solubility of smaller crystals. Two dispersions were synthesized with

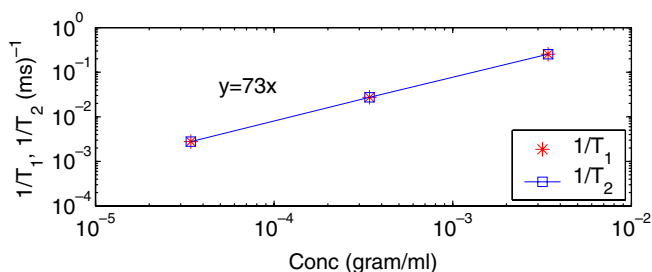


Fig. 6. Longitudinal and transverse relaxation rates ( $\tau_E = 0.2$  ms) of ferric chloride solutions as a function of the concentration of the solution. No echo spacing dependence of  $T_2$  relaxation is observed and  $T_1/T_2$  ratio is equal to unity.

average diameters of the particles equal to 25 and 110 nm. The 25 nm particles were synthesized at 10 °C while 110 nm particles were synthesized at room temperature. Positively charged nanoparticles however, agglomerate in external magnetic fields due to interparticle dipole attractions. Therefore, the nanoparticles were stabilized by adding 1 M Sodium Citrate in the volume ratio of 1%. Stronger columbic repulsion between citrate-coated particles prevents them from agglomeration.

Proton relaxation rates of aqueous dispersions of the citrate-coated particles were measured as a function of the concentration. Fig. 7 shows the plots of longitudinal, transverse and secular relaxation rates with the concentration of the dispersion for the two particle sizes. Linear best fits of the experimental points and the corresponding slopes are also shown. Relaxation rates are linearly dependent on the concentration of the dispersion and no echo spacing dependence of  $T_2$  relaxation rates is observed. Additionally, the  $T_1/T_2$  ratio of magnetite dispersions is greater than one and increases with the particle size. The calculations of characteristic time scales mentioned in Section 6 show that dispersions of submicron particles experience the motionally averaging regime. Thus, no echo spacing dependence of  $T_2$  relaxation is observed and  $T_1/T_2$  ratio increases with the particle size.

### 5.2. Paramagnetic particles on silica surface

NMR proton relaxation measurements with silica sand coated with paramagnetic particles are described in this section. Coated sand serves as a model to quantitatively understand the paramagnetic relaxation mechanisms in porous media. Sand is coated with paramagnetic particles of various sizes and concentrations to illustrate the transition of the relaxation regimes with the length scale of field inhomogeneity.

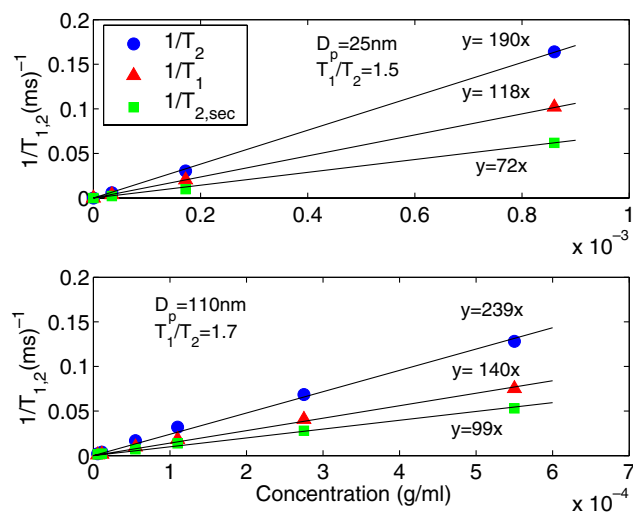


Fig. 7. Plots of transverse, longitudinal and secular relaxation rates with the concentration of aqueous dispersions of magnetite nanoparticles.  $T_2$  relaxation rates are independent of the echo spacing and the  $T_1/T_2$  ratio increases with the particle size.

1. *Fine sand coated with ferric ion:* The following experimental protocol was used to coat fine sand (Sigma Aldrich, grain radius 50  $\mu\text{m}$ ) with paramagnetic ferric ions. Fine sand was repeatedly washed with fresh batches of hydrochloric acid to remove paramagnetic particles originally present on grain surfaces. The sand was then washed with deionized water and dried. A known quantity of the dried sand was kept in contact with acidic (pH 1) solutions of ferric chloride of known concentrations for 24 h in a plastic bottle. The solid to liquid ratio (gm sand/ml) of the slurries was kept at 1:10. Low pH ( $\ll 7$ ) of ferric solutions helps to prevent the precipitation of hydroxides on the sand surface. To ensure uniform coating, the slurries were constantly rotated which prevents the sand from settling at the bottom. After 24 h, the supernatant was removed and the coated sand was repeatedly washed and saturated with deionized water. This last step removes any remaining ferric ions in the pore liquid. Thus, the relaxation of the pore liquid can be attributed only to surface relaxation and to diffusion in internal field gradients.

The surface concentration of the ferric ions can be estimated by measuring the quantity of ferric ions deposited on a known surface area of sand as described. BET surface area of sand (0.2  $\text{m}^2/\text{g}$ ) was determined using  $\text{N}_2$  adsorption at 77 K. To estimate the deposited quantity of ferric ions, relaxation time of the supernatant was measured. Using the calibration between the concentration and relaxation rate of ferric chloride solution (Fig. 6), the concentration of the supernatant can be determined. The difference in the concentration of the supernatant and the original coating solution multiplied by the volume of the solution gives the quantity of ferric ions deposited on the sand surface.

Fig. 8 shows  $T_1$  and  $T_2$  distributions of the water-saturated sand coated with ferric ions at various surface concentrations expressed as surface area/ion. Both  $T_1$  and  $T_2$  relaxation times decrease as the surface concentration of  $\text{Fe}^{3+}$  ions increases. However, no echo spacing dependence of  $T_2$  relaxation is observed and the  $T_1/T_2$  ratio of coated sand is close to that of washed sand (1.26) at all concentrations. Two important conclusions can be deduced from these observations:

- I. Surface relaxation increases as the concentration of ferric ions on silica surface increases as shown by the corresponding decrease in  $T_1$  and  $T_2$  relaxation times. This conclusion is also consistent with the observations that longitudinal and transverse relaxivities of porous media increase with the concentration of paramagnetic particles on pore surfaces [19,31].
- II.  $T_2$  relaxation due to dephasing in inhomogeneous field induced by  $\text{Fe}^{3+}$  ions is negligible. Secular relaxation is proportional to the square of the size of paramagnetic particle in the motionally averaging regime (valid for  $\text{Fe}^{3+}$ , Section 6) and is negligible for angstrom sized ferric ions.

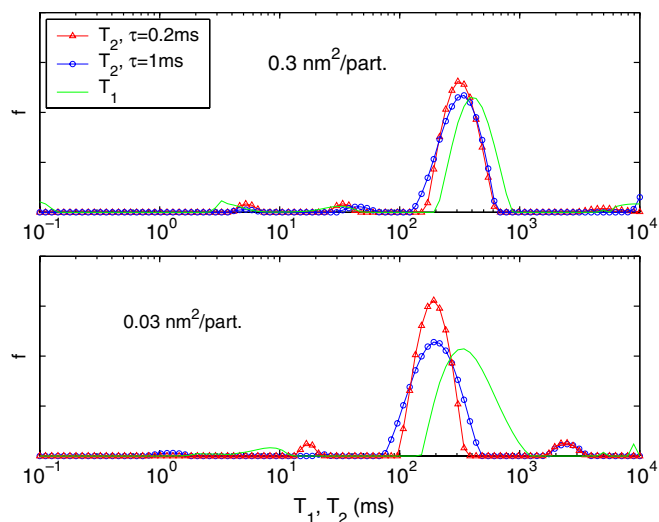


Fig. 8.  $T_1$  and  $T_2$  distributions of fine sand coated with ferric ions at different surface concentrations. No echo spacing dependence of  $T_2$  relaxation is observed and  $T_1/T_2$  is same as that of uncoated sand.

These conclusions are however, contingent on the condition that paramagnetic particles are present in dilute surface concentrations. Kenyon et al. [32] showed that surface relaxivities obtain asymptotic values at high concentration of paramagnetic particles. Similarly, secular relaxation can become significant at high concentration of particles due to superposition of fields induced by individual particles.

2. *Fine sand coated with magnetite nanoparticles:* Known quantity of the fine sand was coated with positively charged 25 and 110 nm magnetite particles by following the same procedure as was used for coating ferric ions. The concentrations of the coating dispersions were varied to obtain different surface concentrations of magnetite. The coated sand was washed and saturated with deionized water. Note that the coating is done with positively charged magnetite *not* coated with citrate ion. Figs. 9 and 10 show the  $T_1$  and  $T_2$  distributions of water-saturated fine sand coated with 25 and 110 nm magnetite at different surface concentrations (surface area/particle).

At low surface concentrations of either 25 or 110 nm particles no echo spacing dependence of  $T_2$  relaxation is observed. At high concentrations however, echo spacing dependence of  $T_2$  relaxation is observed for both cases. This transition in echo spacing dependence can be understood in terms of the length scales of field inhomogeneity. Fig. 1 shows that at low concentration, field inhomogeneity extends to length scale comparable to the size of paramagnetic particles. Thus, for submicron paramagnetic particles, field inhomogeneities are motionally averaged in time much smaller than  $\tau_E$  ( $\tau_R < \tau_E$ , Section 6) and  $T_2$  relaxation shows no echo spacing dependence. At high concentrations, the particles form a shell around silica grains such that the length scale of field inhomogeneity is comparable to the grain

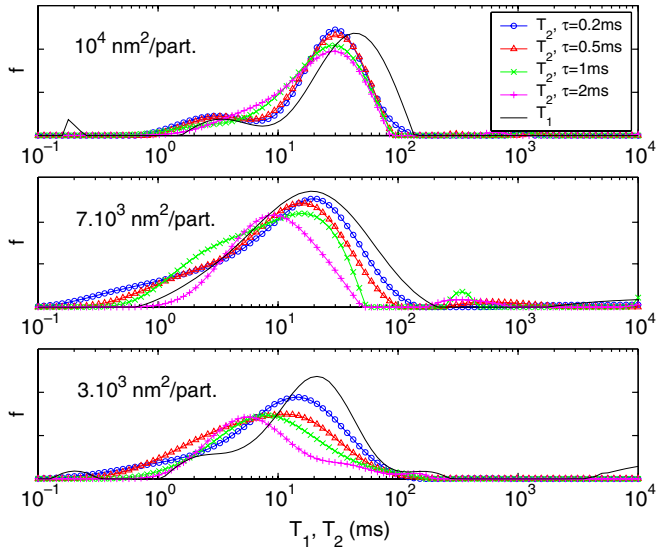


Fig. 9.  $T_1$  and  $T_2$  distribution of water-saturated fine sand coated with 25 nm magnetite nanoparticles at various concentrations.

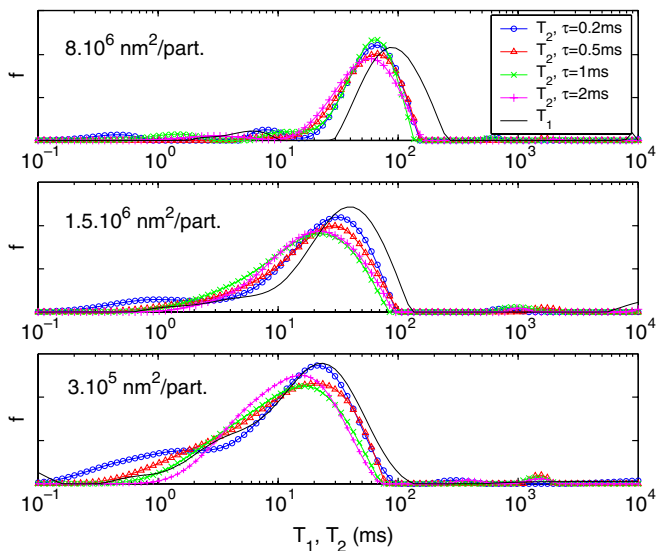


Fig. 10.  $T_1$  and  $T_2$  distribution of water-saturated fine sand coated with 110 nm magnetite nanoparticles at various concentrations.

size (Fig. 2). Due to large size of the substrate silica grain, field inhomogeneities are *not* motionally averaged and hence, echo spacing dependence of  $T_2$  relaxation is observed. A quantitative calculation of the characteristic time scales is shown in Section 6 to corroborate these assertions.

3. *Fine sand with dispersed 2.4  $\mu\text{m}$  magnetite:* The length scale of field inhomogeneity can also be increased by increasing the size of the paramagnetic particle. Fine sand was dispersed with 2.4  $\mu\text{m}$  magnetite (Fischer Scientific) dispersions of known concentrations. Fig. 11 shows  $T_1$  and  $T_2$  distribution of water-saturated fine sand with dispersed 2.4  $\mu\text{m}$  magnetite at two concentrations. A strong dependence of transverse relaxation on echo spacing is observed and the  $T_1/T_2$  ratio is greater

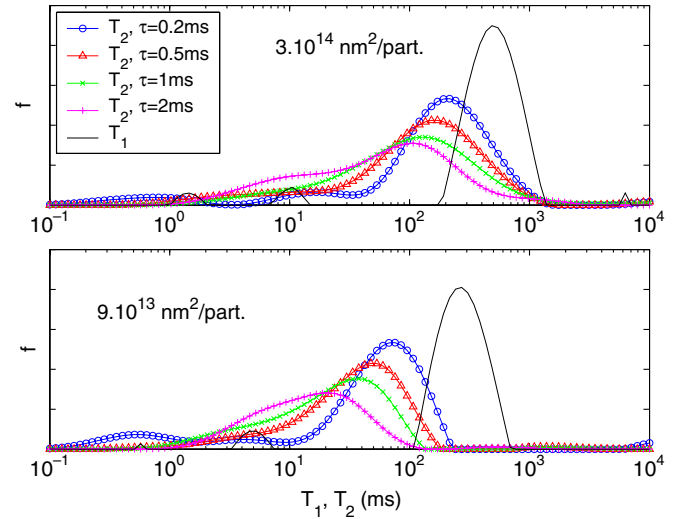


Fig. 11.  $T_1$  and  $T_2$  distributions of fine sand with dispersed 2.4  $\mu\text{m}$  magnetite at two concentrations. A large  $T_1/T_2$  ratio and echo spacing dependence of transverse relaxation is observed.

than 2. These observations are also expected since the field inhomogeneity for micron size particles is not motionally averaged in time for echo formation.

4. *Coarse sand coated with magnetite nanoparticles:* Another set of NMR experiments were performed with coarse sand (Ottawa Sand 20/40 mesh) coated with magnetite nanoparticles. At high surface concentration of paramagnetic particles, the range of Larmor frequencies ( $\delta\omega_{\text{shell}}$ ) varies inversely with the radius of the substrate silica grain (Eq. (29)). Thus, the transition of relaxation regimes can also be quantitatively studied by changing the size of the silica grain.

Coarse sand was washed with Hydrochloric acid to remove any originally present paramagnetic minerals. Washed sand was then coated with 25 nm magnetite particles by following the same procedure as was used for coating fine sand. Fig. 12 shows  $T_1$  and  $T_2$  distributions of water-saturated coarse sand coated with 25 nm magnetite at different surface concentrations. The distributions show similar characteristics as that observed for coated fine sand. At the lowest concentration ( $4 \times 10^3 \text{ nm}^2/\text{particle}$ ), no echo spacing dependence of transverse relaxation is observed. However, at high concentration ( $7 \times 10^2 \text{ nm}^2/\text{particle}$ ), echo spacing dependence of  $T_2$  relaxation is observed. These results suggest that the system transitions from the motionally averaging regime at low concentrations to either the localization or the free diffusion regime at higher concentrations.

## 6. Paramagnetic relaxation in sandstones

A quantitative interpretation of the experimental results in terms of characteristic time scales and asymptotic regimes is described in this section. We first calculate the characteristic time scales for paramagnetic ferric ions and

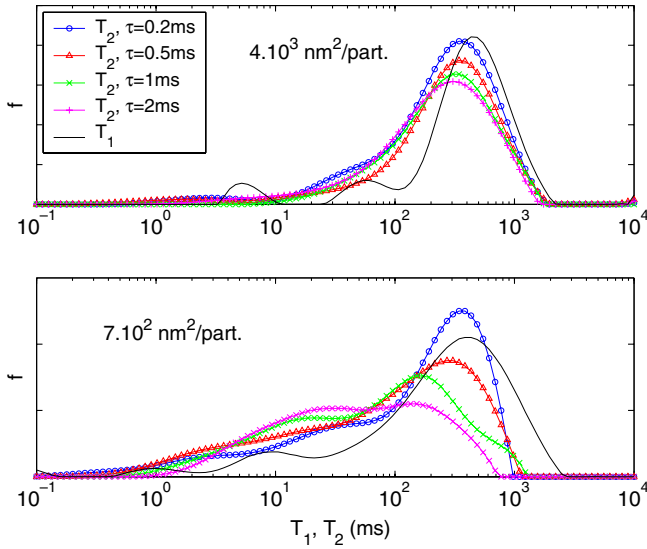


Fig. 12.  $T_1$  and  $T_2$  distributions of coarse sand coated with 25 nm magnetite at various concentrations.

magnetite nanoparticles in dispersion. These calculations in turn help to quantify the relaxation characteristics of the model sandstones.

### 6.1. Characteristic time scales for paramagnetic particles

As was described in Section 2, secular relaxation can be characterized by three regimes depending on the shortest characteristic time scale. In motionally averaging regime, the secular relaxation rate is independent of the echo spacing and increases with the particle size and concentration (Eq. (17)). Similar relaxation characteristics are also observed for aqueous dispersions of submicron paramagnetic particles as shown in Figs. 6 and 7. Thus, it can be hypothesized that proton relaxation in aqueous dispersions of (submicron) paramagnetic particles experiences motionally averaging regime. To prove the validity of the hypothesis, characteristic time scales ( $\tau_E, \tau_R, \tau_\omega$ ) need to be quantitatively evaluated. The value of  $\tau_E$  is known from the experimental measurements. In this study, the smallest  $\tau_E$  used was 0.2 ms. The diffusional correlation time ( $\tau_R$ ) can be calculated from the radius of the paramagnetic particle ( $R_0$ ) and diffusivity of water at 30 °C ( $\sim 2.5 \times 10^{-5}$  cm<sup>2</sup>/s) by using Eq. (11). Under the assumption of motionally averaging regime, the expression for the secular relaxation rate (Eq. (17)) can be used to estimate  $\delta\omega$  for the magnetite nanoparticles as shown below.

$$\frac{1}{T_{2,\text{sec}}} = \frac{16}{405} \Phi \delta\omega^2 \tau_R = \frac{16\delta\omega^2 \tau_R}{405d} C \quad (48)$$

Here  $C$  is the concentration of the dispersion, and  $d$  is magnetite density. Thus,  $\delta\omega$  (rad/s) for the 25 and 110 nm magnetite dispersions can be evaluated from the slope ( $s$ ) of the plot between the secular relaxation rate and the concentration (Fig. 7) as

$$\delta\omega = \sqrt{\frac{405sdD}{16R_0^2}} \quad (49)$$

$\tau_\omega$  is obtained as the reciprocal of  $\delta\omega$ . For ferric ions,  $\delta\omega$  can be calculated from Eq. (10) using  $\chi_{\text{Fe}^{3+}} = 0.00046$  [33] and  $\gamma B_0 = 2$  MHz. Table 1 lists the characteristic time scales for the different particles. For all cases,  $\tau_R < \tau_\omega$  and  $\tau_R < \tau_E$  (except for 110 nm particle for which  $\tau_R \sim \tau_\omega$ ) and thus, the earlier hypothesis of motionally averaging regime is justified.

The condition  $\tau_R < \tau_E$  implies that the magnetic field inhomogeneities are motionally averaged in time shorter than  $\tau_E$ . Thus, no dependence of  $T_2$  relaxation on echo spacing is observed for the aqueous dispersions of ferric ions and magnetite nanoparticles. Additionally, secular relaxation rate is proportional to the square of the radius of the paramagnetic particle in the motionally averaging regime (Eq. (17)). Due to small size of the ferric ion, secular relaxation contributes negligibly to the transverse relaxation and thus, the  $T_1/T_2$  ratio of ferric solutions is unity. (This is true for low magnetic fields such that  $\delta\omega\tau_R < 1$ ). Secular relaxation however, increases for the larger particles and contributes significantly to the  $T_2$  relaxation. Thus, the  $T_1/T_2$  ratio of magnetite dispersions increases with the particle size.

### 6.2. Relaxation regimes in sandstones

The relaxation time distributions of model sandstones shown in Figs. 8–12 illustrate the transition of relaxation regimes with change in governing parameters such as the size and concentration of paramagnetic particles. This transition of relaxation regimes can be interpreted by employing the calculations of characteristic time scales of Table 1.

1. *Motionally averaging regime*: This regime is experimentally observed for fine sand coated with ferric ions and for fine and coarse sand coated with 25 and 110 nm magnetite particles at low concentrations. For these cases, no echo spacing dependence of  $T_2$  relaxation is observed and the  $T_1/T_2$  ratio is higher than that of washed sand (except for  $\text{Fe}^{3+}$  coated sand). At low surface concentrations, superposition of internal fields induced by individual particles is insignificant (Fig. 1). Thus, protons in the pore fluid dephase as if diffusing in internal field induced by individual particles. Since  $\tau_R$  is the shortest characteristic time for the submicron particles (Table 1), field

Table 1  
Characteristic time scales for the aqueous dispersions of ferric ions and magnetite nanoparticles

Time scale (s)	0.12 nm $\text{Fe}^{3+}$	25 nm Magnetite	110 nm Magnetite
$\tau_R$	$3 \times 10^{-11}$	$6 \times 10^{-8}$	$10^{-6}$
$\tau_{E,\text{min}}$	$2 \times 10^{-4}$	$2 \times 10^{-4}$	$2 \times 10^{-4}$
$\tau_\omega$	$2 \times 10^{-4}$	$8 \times 10^{-8}$	$3 \times 10^{-7}$

inhomogeneities are motionally averaged and no echo spacing dependence is observed. The  $T_1/T_2$  ratio is higher than that of washed sand due to additional contribution of secular relaxation to  $T_2$  relaxation.

These experimental results also explain the wide range of the  $T_1/T_2$  ratio in sandstones with no echo spacing dependence of the  $T_2$  relaxation [34,35]. In motionally averaging regime, secular relaxation increases with the size and susceptibility of the paramagnetic particle (Eq. (17)). Thus, the presence of paramagnetic minerals of various sizes and susceptibilities on pore surfaces of sandstones can result in a range of  $T_1/T_2$  ratio. Since the diffusional correlation time is much shorter than the time for echo formation in this regime, no echo spacing dependence of the  $T_2$  relaxation would be observed. An important conclusion is that the lack of echo spacing dependence of transverse relaxation does *not* necessarily imply that relaxation is not influenced by diffusion effects.

2. *Free diffusion regime*: Free diffusion regime of secular relaxation arises when half echo spacing is the shortest characteristic time compared to  $\tau_R$  and  $\tau_\omega$ . The conditions for free diffusion regime can be satisfied in sedimentary rocks at high surface concentration of paramagnetic particles on silica grains. At high surface concentrations, paramagnetic particles form a shell around silica grains such that the field inhomogeneity extends to large distances proportional to the grain size (Fig. 2). In addition, the range of Larmor frequencies is reduced (compared to that for a single particle) by a factor  $3\varepsilon/R_g$  due to superposition of fields (Eq. (29)). Consequently,  $\tau_R$  and  $\tau_\omega$  increase and may become larger than  $\tau_E$  for appropriate system parameters.

The free diffusion regime is observed experimentally for fine sand coated with 110 nm magnetite and coarse sand coated with 25 nm magnetite at surface concentrations  $1.5 \times 10^6$  and  $7 \times 10^2$  nm<sup>2</sup>/particle, respectively. Table 2 lists the characteristic time scales for the two cases.  $\tau_\omega$  is obtained from the reciprocal of  $\delta\omega_{\text{shell}}$  (Eq. (29)) where the thickness of the shell is calculated such that the volume of the shell is the same as the total volume of particles deposited on a single silica grain.  $\tau_R$  is calculated using Eq. (5) where the length scale of inhomogeneity ( $L$ ) is assumed to be the radius of the interstitial pore between silica grains (Eq. (30)). For both cases,  $\tau_E$  is the shortest time scale and thus, the conditions for free diffusion regime are satisfied. Fig. 14 shows that echo

spacing dependence of the secular relaxation rates in the free diffusion regime is approximately quadratic as predicted by Eq. (23).

3. *Localization regime*: Localization regime arises when the time for significant dephasing ( $\tau_\omega$ ) is the shortest characteristic time. This condition can also be satisfied at high surface concentrations of paramagnetic particles if the frequency range for spherical shell is large such that  $\tau_\omega$  (reciprocal of  $\delta\omega$ ) is short compared to  $\tau_R$  and  $\tau_E$ .

Localization regime is experimentally observed for fine sand coated with 25 nm ( $3 \times 10^3$  nm<sup>2</sup>/particle) and 110 nm ( $3 \times 10^5$  nm<sup>2</sup>/particle) at the highest surface concentrations. Table 3 shows the characteristic time scales for the two cases. (Time scales  $\tau_\omega$  and  $\tau_R$  are calculated using the same method as that used for the free diffusion regime). For both cases, the conditions for localization regime ( $\tau_\omega < \tau_R$  and  $\tau_\omega < \tau_E$ ) are satisfied. Localization regime can also be observed for relaxation in the presence of large paramagnetic particles with large diffusional correlation time. This is the case for relaxation in fine sand with dispersed 2.4  $\mu\text{m}$  magnetite (Fig. 12). The values of the characteristic times for 2.4  $\mu\text{m}$  magnetite are also mentioned in Table 3 ( $\delta\omega$  is assumed to be same as that for 110 nm particles). The conditions for localization regime are again satisfied and thus, echo spacing dependence of transverse relaxation is observed.

An example of localization regime is transverse relaxation in North Burbank (NB) sandstone with macropores lined with chlorite clay flakes. Large field gradients are concentrated around the sharp corners of the clay flakes and in the micropores between clay flakes. The gradients also extend considerably in the macropore although the strength is not as high as in micropores [36]. Fluid molecules in the micropores and macropores are, however, coupled by diffusion [37]. Thus, in general, the molecules experience gradients that are intermediate to those in the micro and macropores. Fig. 13 shows the  $T_1$  and  $T_2$  distributions of a water-saturated North Burbank sandstone core. Once again, a large  $T_1/T_2$  ratio is observed and the  $T_2$  distributions show echo spacing dependence.

The values of characteristic time scales need to be evaluated to characterize the relaxation regime in the North Burbank sandstone. The pore size distribution obtained from mercury porosimetry [37] shows that the average

Table 2

Time scales for relaxation in coarse sand coated with 25 nm ( $7 \times 10^2$  nm<sup>2</sup>/particle) and fine sand coated with 110 nm magnetite ( $1.5 \times 10^6$  nm<sup>2</sup>/particle)

Time scale (s)	25 nm	110 nm
$\tau_R$	1.07	0.05
$\tau_{E,\text{min}}$	$2 \times 10^{-4}$	$2 \times 10^{-4}$
$\tau_\omega$	$9 \times 10^{-4}$	$1.3 \times 10^{-3}$

Table 3

Time scales for systems experiencing the localization regime

Time scale (s)	25 nm	110 nm	2.4 $\mu\text{m}$	NB
$\tau_R$	0.05	0.05	$6 \times 10^{-4}$	0.2
$\tau_{E,\text{min}}$	$2 \times 10^{-4}$	$2 \times 10^{-4}$	$2 \times 10^{-4}$	$1.6 \times 10^{-4}$
$\tau_\omega$	$5 \times 10^{-5}$	$5 \times 10^{-5}$	$3 \times 10^{-7}$	$5 \times 10^{-5}$

The surface concentrations for coated sand experiments are 25 nm ( $3 \times 10^3$  nm<sup>2</sup>/part), 110 nm ( $3 \times 10^5$  nm<sup>2</sup>/part.) and 2.4  $\mu\text{m}$  magnetite ( $3 \times 10^{14}$  nm<sup>2</sup>/part,  $9 \times 10^{13}$  nm<sup>2</sup>/part.).

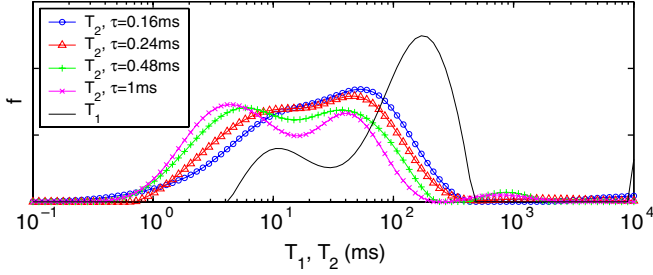


Fig. 13.  $T_1$  and  $T_2$  distributions of water-saturated North Burbank sandstone core.

macropore radius ( $R_p$ ) is 24  $\mu\text{m}$  assuming a pore-body to pore-throat ratio of 3. Thus, the diffusional correlation time ( $\tau_R$ ) is equal to 0.2 s using Eq. (7). For a pore with average gradient  $g$ , the range of frequencies is given as

$$\delta\omega \sim 2\gamma g R_p \quad (50)$$

From the numerical calculations of Zhang et al. [36],  $\delta\omega$  for North Burbank is estimated to be  $2 \times 10^4$  rad/s. Since  $\tau_E \geq 10^{-4}$  s, both conditions for the localization regime ( $\delta\omega\tau_R \gg 1$ ,  $\delta\omega\tau_E \gg 1$ ) are satisfied for the core. The characteristic time scales are mentioned in Table 3.

Fig. 14 summarizes the echo spacing dependence of the experimental systems in the free diffusion and/or localization regime on the plot of the secular relaxation rates with  $\delta\omega\tau_E$ . The dashed line is the boundary  $\delta\omega\tau_E = 1$  delineating the two regimes. The solid lines are the regression lines for the power-law fits between the relaxation rates and  $\delta\omega\tau_E$ . The relaxation rates show approximately quadratic dependence on  $\delta\omega\tau_E$  in the free diffusion regime ( $\delta\omega\tau_E < 1$ ). In contrast, the dependence of relaxation rates on  $\delta\omega\tau_E$  is less than linear in the localization regime ( $\delta\omega\tau_E > 1$ ). This less than linear dependence of the secular relaxation rates on

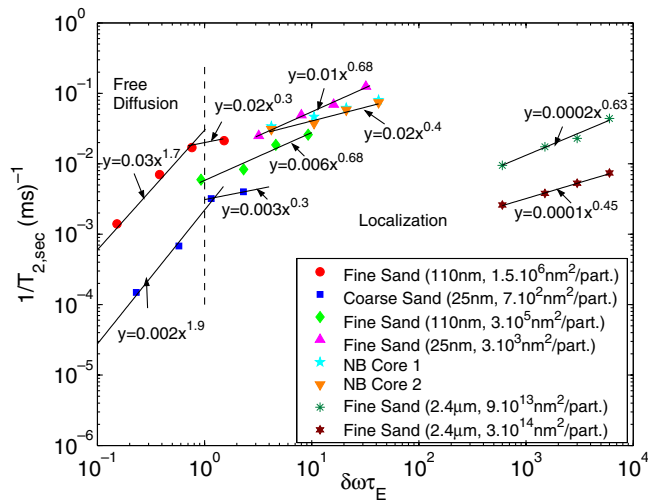


Fig. 14. Plot of secular relaxation rates with  $\delta\omega\tau_E$  for experimental systems in free diffusion and localization regimes. The relaxation rates show nearly quadratic dependence on echo spacing in the free diffusion regime and less than linear dependence in the localization regime.

$\tau_E$  in the localization regime was also illustrated in the numerical simulations of Section 4 (Fig. 5). These results can also explain the initially linear echo spacing dependence of transverse relaxation rates in porous media observed by Brown et al. [27] and Fantazzini et al. [28]. Power-Law fits between the simulated relaxation rates and  $\delta\omega\tau_E$  in the localization regime of Fig. 5 show that the echo spacing dependence is nearly quadratic for small values of  $\delta\omega\tau_E$  ( $1 < \delta\omega\tau_E < 5$ ). However, the dependence is less than linear for higher values of  $\delta\omega\tau_E$  ( $10^2 < \delta\omega\tau_E < 10^3$ ). Thus, a linear dependence on echo spacing can be observed for intermediate values of  $\tau_E$  in the localization regime.

The relaxation characteristics of the experimental systems can be summarized on the contour map of dimensionless secular relaxation rates in  $(\delta\omega\tau_R, \delta\omega\tau_E)$  parameter space. The dimensionless rates for the experimental systems are estimated by normalizing the dimensional secular relaxation rates (Eq. (1)) by the characteristic rate ( $1/t_0$ ) as shown

$$\frac{1}{T_{2,\text{sec}}^D} = \frac{1}{T_{2,\text{sec}}} \bigg/ \frac{1}{t_0} = \left( \frac{1}{T_2} - \frac{1}{T_1} \right) \left( \frac{3}{\Phi\delta\omega} \right) \quad (51)$$

The longitudinal and transverse relaxation times are obtained from the modes of corresponding  $T_1$  and  $T_2$  distributions. Four parameters  $\delta\omega$ ,  $\tau_R$ ,  $\tau_E$ ,  $\Phi$  are required for the calculation of dimensionless rates and the corresponding coordinates  $(\delta\omega\tau_R, \delta\omega\tau_E)$ . The parameters  $\delta\omega$ ,  $\tau_R$  and  $\tau_E$  are obtained from Tables 1–3 ( $\delta\omega = 1/\tau_\omega$ ). The paramagnetic volume fraction  $\Phi$  is equal to 0.6 at high surface concentrations of paramagnetic particles and is equal to the ratio of paramagnetic particles to total volume at low concentrations. Fig. 15 shows the dimensionless secular relaxation rates in the  $(\delta\omega\tau_R, \delta\omega\tau_E)$  parameter space for the experimental systems. The relaxation rates for magnetite dispersions and sand coated with paramagnetic particles at low concentrations are compared with the simulations for  $\Phi \leq 1.25 \times 10^{-4}$  (upper panel). The relaxation rates for sand coated with higher concentrations of paramagnetic particles and North Burbank are compared with simulations for  $\Phi = 0.6$  (lower panel). (For the simulations with  $\Phi = 0.6$ , field distribution is specified by Eq. (28) for a paramagnetic shell of susceptibility 0.2 (SI units) and assuming  $3\epsilon/R_g = 10^{-3}$ . The relaxation rates can not be simulated for  $\delta\omega\tau_E > 50$  due to dephasing of random walkers). A good quantitative agreement between the theoretically predicted rates and experimentally measured rates is observed for all cases.

The relaxation characteristics of the experimental systems in Fig. 15 can be explained in terms of the asymptotic regimes. The aqueous dispersions of nanoparticles and fine and coarse sand coated with 25 and 110 nm at low surface concentrations (\*, x symbols) experience motionally averaging regime. Thus, no echo spacing is observed. Experiments with fine sand coated at high concentrations of 25 nm (open and closed triangles) and 110 nm (open and closed

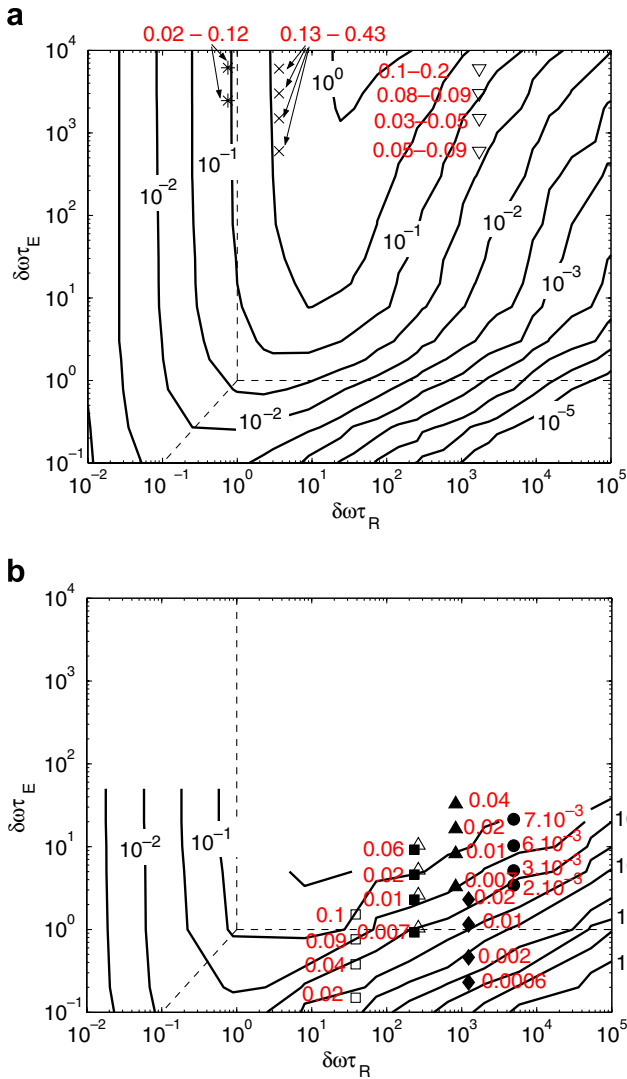


Fig. 15. Parametric representation of dimensionless secular relaxation rates for experimental systems in the  $(\delta\omega\tau_R, \delta\omega\tau_E)$  parameter space. The symbols are the experimental systems: (\*) fine and coarse sand coated with dilute concentrations of 25 nm, (x) fine sand coated with dilute surface concentration of 110 nm magnetite, ( $\Delta$ ) fine sand coated with 25 nm magnetite Conc. =  $7 \times 10^3$  nm<sup>2</sup>/part., ( $\blacktriangle$ ) fine sand coated with 25 nm magnetite Conc. =  $3 \times 10^3$  nm<sup>2</sup>/part., ( $\blacklozenge$ ) coarse sand coated with 25 nm magnetite Conc. =  $7 \times 10^2$  nm<sup>2</sup>/part., ( $\square$ ) fine sand coated with 110 nm magnetite Conc. =  $1.5 \times 10^6$  nm<sup>2</sup>/part., ( $\blacksquare$ ) fine sand coated with 110 nm magnetite Conc. =  $3 \times 10^5$  nm<sup>2</sup>/part., ( $\nabla$ ) fine sand with dispersed 2.4  $\mu$ m magnetite, ( $\bullet$ ) North Burbank sandstone. (a) Comparison with contour plots for  $\Phi \leq 1.25 \times 10^{-4}$  (b) Comparison with contours for  $\Phi = 0.6$ .

squares) lie in localization and free diffusion regimes. Similarly, coarse sand coated with 25 nm at high concentration (closed diamonds) lie in free diffusion and localization regimes. Thus, echo spacing dependence of the  $T_2$  relaxation is observed for these cases. North Burbank sandstone (solid circles) and fine sand with dispersed 2.4  $\mu$ m magnetite (inverted triangles) also fall in localization regime and display an echo spacing dependence. The average absolute deviation between the experimental and simulated values is less than 80% which means that, on an average, the theory

predicts secular relaxation rates within the right order of magnitude.

### 7. Conclusions

The loss of phase coherence between nuclear spins due to diffusion in magnetic field inhomogeneities leads to additional transverse relaxation called “secular” relaxation. A generalized relaxation theory is proposed which identifies three characteristic time scales governing secular relaxation: diffusional correlation time ( $\tau_R$ ), time for significant dephasing ( $\tau_\omega$ ) and half echo spacing of the CPMG sequence ( $\tau_E$ ). The characteristic time scales can be defined for a general inhomogeneous field distribution. Depending on the shortest time scale, secular relaxation can be classified in three asymptotic regimes of motionally averaging, localization and free diffusion.

The asymptotic regimes show different relaxation characteristics. In motionally averaging regime, field inhomogeneities are averaged due to fast diffusion in time much shorter than  $\tau_E$ . Thus, no echo spacing dependence of secular relaxation is observed. In free diffusion regime,  $\tau_E$  is the shortest time scale. Secular relaxation rates show quadratic dependence on echo spacing in this regime. Localization regime is characterized by  $\tau_\omega$  as being the shortest time scale. A sub-linear echo spacing dependence of secular relaxation is observed in this regime. In contrast to motionally averaging regime, relaxation rates in free diffusion and localization regimes are inversely dependent on the length scale of inhomogeneity. The characteristics of the relaxation regimes can be demonstrated in a single contour map of dimensionless relaxation rates in  $(\tau_R/\tau_\omega, \tau_E/\tau_\omega)$  parameter space.

The classification of secular relaxation in asymptotic regimes provides conceptual understanding of relaxation characteristics of porous media. Experiments with sand coated with submicron paramagnetic particles show that the systems transition from the motionally averaging regime at low surface concentrations to either the free diffusion or the localization regime at high surface concentrations. Thus, echo spacing dependence of  $T_2$  relaxation is observed only at sufficiently high surface concentration of paramagnetic particles. This transition in relaxation regimes occurs because the length scale of field inhomogeneity increases at high surface concentrations due to superposition of fields induced by neighboring particles. The relaxation characteristics of asymptotic regimes can also provide explanation for the diverse NMR characteristics observed in fluid-saturated sandstones. A large range of  $T_1/T_2$  ratio in sandstones with no echo spacing dependence of  $T_2$  relaxation observed by Kleinberg et al. [34] can arise in the motionally averaging regime. The quasi or sub-linear dependence of the  $T_2$  relaxation on echo spacing shown in experiments of Fantazzini et al. [28] can arise in the localization regime. Thus, the estimation of characteristic time scales provides quantitative understanding of paramagnetic relaxation in sandstones.

## Appendix. Numerical integration of Bloch equation

A continuous random walk algorithm [22] is applied to model  $T_2$  relaxation of spins (Eqs. (40)–(43)) diffusing in an inhomogeneous internal field  $B_{\delta z}(r, \theta)$ . Random walkers are initially distributed uniformly in an annular region outside a spherical paramagnetic particle. The walkers start with a zero initial phase. In dimensionless time step  $dt^*$ , the  $n$ th walker at a position  $(r^*, \theta)$  accumulates a phase of  $\Delta\phi_n = \omega^*(r^*, \theta)dt^*$ . The dimensionless Larmor frequency  $\omega^*$  is obtained by normalizing the Larmor frequency  $\omega = \gamma B_{\delta z}$  with the characteristic rate  $(1/t_0)$  as shown below

$$\omega^*(r^*, \theta) = \frac{\omega(r, \theta)}{1/t_0} = \frac{(3 \cos^2 \theta - 1)}{r^{*3}} \quad (\text{A.1})$$

After every time step  $dt^*$ , the stochastic diffusion of a walker is simulated by choosing a random displacement with zero mean and standard deviation  $\sqrt{2N_D dt^*}$  in the  $x$ ,  $y$  and  $z$  directions in Cartesian coordinates. The clock is incremented by  $dt^*$  after every time step. At the time of the application of  $\pi$  pulses  $t^* = \tau_E^*, 3\tau_E^*, 5\tau_E^*, \dots$ , the phase of all random walkers is inverted. Perfect reflection at the inner and outer boundaries is simulated by returning the walker to the same position if the next displacement takes it outside the boundaries. The echo intensity at times  $t^* = 2\tau_E^*, 4\tau_E^*, 6\tau_E^*, \dots$  is evaluated by averaging the phase of all walkers

$$M(t^*) = \frac{1}{N} \sum_{n=1}^N \exp(i\phi_n(t^*)) \quad (\text{A.2})$$

where  $N$  is the number of walkers and  $\phi_n(t^*)$  is the phase of the  $n$ th walker at time  $t^*$ . The dimensionless relaxation rate is calculated from the slope of exponential fit to the simulated echo intensities. However, the magnetization decay is multi-exponential for simulations such that  $\delta\omega\tau_R > 1000$ . For such cases, the relaxation rate is calculated from the slowest component of the multi-exponential decay. There are two simulation parameters which should be appropriately chosen to ensure the accuracy of the solution:

1. Number of walkers: Number of walkers determines the statistical noise in the simulations. Simulations with different number of walkers show that  $N=10,000$  gives a good accuracy ( $<1\%$  average absolute deviation from the analytical solutions) and a reasonable amount of computational time.
2. Time step ( $dt^*$ ): The value of the time step should be chosen such that the dimensionless time step  $dt^*$  is less than the (normalized) characteristic time scales of the system.

$$dt^* \ll \frac{\tau_R}{t_0}, \quad dt^* \ll \frac{\tau_\omega}{t_0}, \quad dt^* \ll \frac{\tau_E}{t_0}$$

## References

[1] J. Godward, E. Ciampi, M. Cifelli, P.J. McDonald, Multidimensional imaging using combined stray field and pulsed gradients, *J. Magn. Reson.* 155 (2002) 92–99.

[2] M.J.D. Mallett, M.R. Halse, J.H. Strange, Stray field imaging by magnetic field sweep, *J. Magn. Reson.* 132 (1998) 172–175.

[3] P.M. Glover, P.J. McDonald, B. Newling, Stray-field imaging of planar films using a novel surface coil, *J. Magn. Reson.* 126 (1997) 207–212.

[4] Jay H. Baltisberger, Sabine Hediger, Lyndon Emsley, Multi-dimensional magnetic resonance imaging in a stray magnetic field, *J. Magn. Reson.* 172 (2005) 79–84.

[5] R.N. Muller, P. Gillis, F. Moiny, A. Roch, Transverse relaxivity of particulate MRI contrast media: from theories to experiments, *Magn. Reson. Med.* 22 (1991) 178–182.

[6] P. Hardy, R.M. Henkelman, On the transverse relaxation rate enhancement induced by diffusion of spins through inhomogeneous fields, *Magn. Reson. Med.* 17 (1991) 348–356.

[7] R. Freedman, A. Sezginer, M. Flaum, A. Matteson, S. Lo, G.J. Hirasaki, A New NMR Method of Fluid Characterization in Reservoir Rocks: Experimental Confirmation and Simulation Results, SPE Paper 63214, Society of Petroleum Engineers, Dallas, TX, 2000.

[8] Boqin Sun, In situ fluid typing and quantification with 1D and 2D NMR logging, *Magn. Reson. Imaging* 25 (2007) 521–524.

[9] P. Gillis, S.H. Koenig, Transverse relaxation of solvent protons induced by magnetized spheres: application to ferritin, erythrocytes and magnetite, *Magn. Reson. Med.* 5 (1987) 323–345.

[10] T.M. DeSwiet, P. Sen, Decay of nuclear magnetization by bounded diffusion in a constant field gradient, *J. Chem. Phys.* 100 (1994) 5597–5604.

[11] R.A. Brooks, F. Moiny, P. Gillis, On  $T_2$  shortening by weakly magnetized particles: the chemical exchange model, *Magn. Reson. Med.* 45 (2001) 1014–1020.

[12] P. Gillis, F. Moiny, R.A. Brooks, On  $T_2$ -shortening by strongly magnetized spheres: a partial refocusing model, *Magn. Reson. Med.* 47 (2002) 257–263.

[13] D.A. Menzel, *Fundamental Formulas of Physics*, Prentice Hall, New York, NY, 1955.

[14] C.H. Neuman, Spin echo of spins diffusing in a bounded medium, *J. Chem. Phys.* 60 (1974) 4508–4511.

[15] J.C. Tarczoz, W.P. Halerpin, Interpretation of NMR diffusion measurements in uniform- and nonuniform-field profiles, *Phys. Rev. B* 32 (1985) 2798–2807.

[16] H.Y. Carr, E.M. Purcell, Effects of diffusion on free precession in nuclear magnetic resonance experiments, *Phys. Rev.* 94 (1954) 630–638.

[17] J.H. Jenson, R. Chandra, NMR relaxation in tissues with weak magnetic inhomogeneities, *Magn. Reson. Med.* 44 (2000) 144–156.

[18] P.N. Sen, A. André, S. Axelrod, Spins echoes of nuclear magnetization diffusing in a constant magnetic field gradient and in a restricted geometry, *J. Chem. Phys.* 111 (1999) 6548–6555.

[19] I. Foley, S.A. Farooqui, R.L. Kleinberg, Effect of paramagnetic ions on NMR relaxation of fluids at solid surfaces, *J. Mag. Reson. A* 123 (1996) 95–104.

[20] B.K. Vainshtein, V.M. Fridkin, V.L. Indenbom, *Structure of Crystals*, Springer, 2000.

[21] D.J. Bergman, K.-J. Dunn, NMR of diffusing atoms in a periodic porous medium in the presence of a nonuniform magnetic field, *Phys. Rev. E* 52 (1995) 6516–6535.

[22] R.M. Weisskoff, C.S. Zuo, J.L. Boxerman, B.R. Rosen, Microscopic susceptibility variation and transverse relaxation: theory and experiment, *Magn. Reson. Med.* 31 (1994) 601–610.

[23] H.S. Gutowsky, A. Satka, Dissociation, chemical exchange, and the proton magnetic resonance in some aqueous electrolytes, *J. Chem. Phys.* 21 (1953) 1688–1694.

[24] S. Meiboom, Nuclear magnetic resonance study of the proton transfer in water, *J. Chem. Phys.* 34 (1961) 375–388.

[25] Z. Luz, S. Meiboom, Nuclear magnetic resonance study of the protolysis of triethylammonium ion in aqueous solution—order of the reaction with respect to solvent, *J. Chem. Phys.* 39 (1963) 366–370.

[26] R.A. Brooks,  $T_2$ -shortening by strongly magnetized spheres: a chemical exchange model, *Magn. Reson. Med.* 47 (2002) 388–391.

- [27] R.J.S. Brown, P. Fantazzini, Conditions for initial quasilinear  $T_2^{-1}$  versus  $\tau$  for Carr-Purcell-Meiboom-Gill NMR with diffusion and susceptibility differences in porous media and tissues, *Phys. Rev. B* 47 (1993) 14823–14834.
- [28] P. Fantazzini, R.J.S. Brown, Initially linear echo-spacing dependence of  $1/T_2$  measurements in many porous media with pore scale inhomogeneous fields, *J. Mag. Reson.* 177 (2005) 228–235.
- [29] V. Anand, NMR Oil Well Logging: Diffusional Coupling and Internal Gradients in Porous Media, Ph.D. Thesis, Rice University, 2007.
- [30] R. Massart, Preparation of aqueous magnetic liquids in alkaline and acidic media, *IEEE Transac. Magn.* 17 (1981) 1247–1248.
- [31] J. Chen, NMR Surface Relaxation, Wettability and OBM Drilling Fluids, Ph.D. Thesis, Rice University, 2005.
- [32] W.E. Kenyon, J. Kolleeny, NMR surface relaxivity of calcite with adsorbed  $Mn^{2+}$ , *J. Colloid Interface Sci.* 170 (1994) 502–514.
- [33] R.E. Rosensweig, *Ferrohydrodynamics*, Cambridge University Press, 1985.
- [34] R.L. Kleinberg, S.A. Farooqui, M.A. Horsfield,  $T_1/T_2$  ratio and frequency dependence of NMR relaxation in porous sedimentary rocks, *J. Colloid Interface Sci.* 158 (1993) 195–198.
- [35] R.L. Kleinberg, W.E. Kenyon, P.P. Mitra, Mechanism of NMR relaxation of fluids in rocks, *J. Mag. Reson. A* 108 (1994) 206–214.
- [36] G.Q. Zhang, G.J. Hirasaki, W.V. House, Internal field gradients in porous media, *Petrophysics* 44 (2003) 422–434.
- [37] V. Anand, G.J. Hirasaki, Diffusional coupling between micro and macropores for NMR relaxation in sandstones and carbonates, *Petrophysics* 48 (2007) 289–307.